Hindawi
International Journal of Antennas and Propagation
Volume 2023, Article ID 5516412, 15 pages
https://doi.org/10.1155/2023/5516412

Research Article

A Contact-Less Electrically Small Antenna Sensor for Retinal Cancer Cell Detection

Shaik Rizwan, Kanaparthi V. Phani Kumar, P. Sandeep Kumar, and Sachin Kumar

Diagnostics, Therapeutics and Assistive Devices Laboratory, Department of Electronics and Communication Engineering, Faculty of Engineering and Technology, SRM Institute of Science and Technology, Kattankulathur, Tamil Nadu 603203, India

Correspondence should be addressed to Kanaparthi V. Phani Kumar; kvphanikumar264@gmail.com and P. Sandeep Kumar; vrpchs@gmail.com

Received 19 June 2023; Revised 9 October 2023; Accepted 16 October 2023; Published 27 October 2023

Academic Editor: Raffaele Solimene

A new noninvasive and portable diagnostic system for detecting ocular tumors has been proposed. The system uses a contact-less electrically small antenna sensor to detect retinal cancer cells. The antenna sensor is operated in the ISM (Industrial, Scientific, and Medical) 2.413 GHz band and has electrical dimensions of $8 \times 16.2 \times 0.35\ mm^3$. The antenna sensor is fabricated on a biodegradable Teslin substrate and tested in an eye-mimicking phantom to compare numerical computations with measurements. The specific absorption rate (SAR) obtained at near and far-field distances under 1 g of tissue is 1.18 W/kg and 0.353 W/kg, and that under 10 g of tissue is 0.112 W/kg and 0.313 W/kg, respectively. Furthermore, to detect the ocular tumor using the proposed antenna sensor, the resonance frequency shift, and the unsupervised machine learning technique, principle component analysis (PCA) is employed on simulated and measured results. The resonance frequency shift for a 3.5 mm radius tumor is 70 MHz for a single tumor and 120 MHz for double tumors. The PCA generates clusters with and without tumors on the positive and negative sides of the two-dimensional plot. The proposed techniques are more impactful in distinguishing between healthy and malignant tissues. The proposed systematic approach could be a portable platform for early detection of cancerous cells inside the eye.

1. Introduction

An ocular tumor is a tumor that develops in the eye, usually in the interior region of the eye. It is a common malignancy that can afflict anyone at any age with no prior history, especially in children under the age of four, and it is even more common in children under the age of one year. According to the American Cancer Society, there are 3360 new cases of eye cancer in the United States in 2022, with 410 deaths [1, 2]. Malignant tumors are formed in different locations of the vitreous humor, most commonly in the eyelids, as shown in Figure 1. The tumor can damage vision, and it can be spread through the optic nerve to the brain and other regions of the body. Therefore, the spread and death rate due to this ocular tumor can be reduced by early diagnosis. Traditional methods such as magnetic resonance imaging (MRI), computed tomography (CT), ultrasound, and optical coherence tomography (OCT) are useful for tumor diagnosis. However, these methods have substantial limitations. The MRI operates on a lower frequency range, which requires expensive equipment, a long study time, and loud noises. The CT uses an X-ray generator, which exposes the body to more radiation, and expensive and contrast material, potentially worsening renal function in patients with kidney disease [3–5]. Ultrasound scans and OCT are noninvasive methods. Unlike other scanning methods, they do not expose patients to radiation, have no adverse effects, and are often painless. Ultrasound images, on the other hand, are not as detailed as CT or MRI scans. Ultrasound cannot identify if a tumor is cancerous or not, as sound waves are highly attenuated by multiple layers of the human body. The OCT employs light waves rather than sound waves

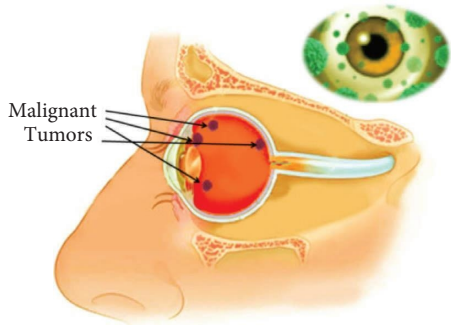

Figure 1: The malignant tumors in different locations of the eye.

like ultrasound; however, their medium opacity can limit optimal imaging and depth limitation of 1–4 mm [6–8].

The present-day clinical diagnostic methods impose various challenges. In summary, mobility, affordability, and safety are the main issues with current approaches. The aforementioned constraints prompted the researchers to develop simplified diagnosis methods using microwaves. Microwaves can easily pass through various human body tissues with different dielectric properties without being attenuated. This characteristic of microwaves makes planar antennas ideal for biomedical applications. The International Telecommunication Union (ITU) has suggested that the frequency band of 2.45–2.5 GHz (ISM band) can be utilized for biomedical applications.

Several research studies on the applications of biomedical systems using planar antennas for off-body, on-body, and inside-the-body communication have been reported in the open literature. In [9], the authors presented a triple-band wearable monopole antenna designed for Internet of Medical Things (IoMT) applications, aimed at facilitating wireless wearable sensors for vital sign monitoring on the human body. The reported antenna utilizes a coplanar waveguide feed and incorporates an artificial magnetic conductor (AMC) array structure, enabling effective operation across three frequency bands. A noninvasive microwave-based system for detecting glucose levels in aqueous solutions was reported in [10]. The reported system employs two RF microstrip patch antennas resonating at 2.4 GHz and 5.7 GHz, fabricated on an FR-4 substrate. An inverted Ω-shaped planar antenna designed for wearable applications, operating at 2.45 GHz ISM band, was proposed in [11]. The reported antenna is constructed using Rogers RO3006 with a 1.27 mm thickness substrate and features an inverted Ω-shaped radiating element connected to a fork-shaped stub. Also, it is microstrip-fed and has a partial ground on the backside. In [12], the authors reported a coplanar waveguide-fed rectenna system designed for efficient RF energy harvesting at 2.4 GHz for Bluetooth/WLAN applications, with dimensions of $40 \times 35\ \text{mm}^2$. The antenna features a rectangular patch with four slots on the radiator and ground slots near the feed line to enhance impedance bandwidth, providing a gain of 4.12 dBi. A compact monopole antenna working in the ISM band was presented in [13], which detects bone fractures based on a resonant frequency shift. An embroidered meander dipole antenna was proposed for real-time breath monitoring [14], and its working principle was based on the resonant frequency shift caused by the chest expansion and the displacement of the lungs during breathing. Furthermore, the planar antennas operated at ISM bands for off-body and inside-the-body communication have been reported in [15–20]. The aforementioned works deals with various developments in planar microwave antenna technology for medical and communication applications. These developments showcase advancements in antenna technology for diverse healthcare and wireless communication applications.

In this paper, a planar microwave antenna sensor is designed to operate the ISM band (2.45 GHz) for off-body communication. The antenna sensor is developed using a meandered microstrip line and acts as an effective compact radiator with reduced resonant resistance. A meandered resonator, tapered feed, and U-shaped notches are loaded on the patch and ground plane to achieve the desired resonating band. A simplified multilayered canonical (SMC) eye model is developed in a full-wave simulator to analyze the performance of the proposed antenna sensor to detect the ocular tumor. The experimental validation is also performed with eye-mimicking phantom.

Table 1 summarizes the geometrical dimensions, volume, electrical size, and impedance bandwidth of recently reported antennas. It shows that, while subject to their clinical applicability, electrical size, overall size, volume, and impedance bandwidth, the recently reported antennas still need to be low profile or compact compared to the proposed asymmetric planar strip- (APS-) fed monopole antenna sensor.

This paper is organized as follows. Section 2 describes the design, evolution, performance, and free space simulated and measured results of the antenna sensor. Section 3 provides a brief description of the inhomogeneous eye modeling and testing using simulation and the experimental setup. Section 4 discusses a brief conclusion of the presented work.

2. Proposed Antenna Sensor Design

The objective is to design a compact ISM-band monopole antenna sensor for detecting ocular malignancy. The proposed antenna sensor is designed on the biodegradable Teslin substrate of permittivity (ϵ_r) of 2.2, thickness of 0.35 mm, and loss tangent (δ) of 0.022. Figure 2 depicts the geometry of the proposed APS-fed antenna, and the size of the antenna is $8 \times 16.2 \times 0.35\ \text{mm}^3$. The antenna configuration has a small footprint of $45.36\ \text{mm}^3$. The antenna consists of a modified ground plane and L-shaped and inverted U-shaped resonators, and it resonates at 2.45 GHz with an impedance bandwidth of 2.29–2.58 GHz. The evolution of the proposed monopole antenna is depicted in Figures 3(a)–3(d).

2.1. Antenna Sensor Evolution. Initially, an APS-fed monopole with an inverted U-shaped strip (antenna-1) is designed to operate at 3.34 GHz, as shown in Figure 3(a). To

Table 1: Comparative analysis among planar microwave antennas for off-body communication.

Ref. (year)	Antenna size ($W \times L \times H$) (mm^3)	Volume (mm^3)	Dielectric constant	Antenna type	Electrically small	Operating frequency (GHz)	Operating bandwidth @ $S_{11} < -10$ dB (MHz)
[13] (2022)	$30 \times 32 \times 1.6$	1536	4.4	Monopole	No	2.45	115
[14] (2022)	$45 \times 4.87 \times 0.464$	101.7	1.3	Meandered dipole	No	2.4	340
[15] (2022)	$7.4 \times 24.7 \times 1.6$	292.45	4.3	CPW-fed monopole	Yes	2.42, 4.5, 5.5	60,1580
[16] (2022)	$13.5 \times 23 \times 1.6$	496.8	4.3	ACS-fed monopole	Yes	2.4, 5.8, 6.78	270, 340, 180
[17] (2023)	$18 \times 30 \times 0.79$	426.6	2.2	CPW-fed antenna	No	2.5, 5.4	550, 650
[10] (2023)	$40 \times 40 \times 1.6$	2560	4.3	Microstrip patch antenna	No	2.5, 5.7	220, 1230
Proposed	$8 \times 16.2 \times 0.35$	45.36	2.2	APS-fed monopole	Yes	2.413	342

ACS: asymmetric coplanar strip; CPW: coplanar waveguide.

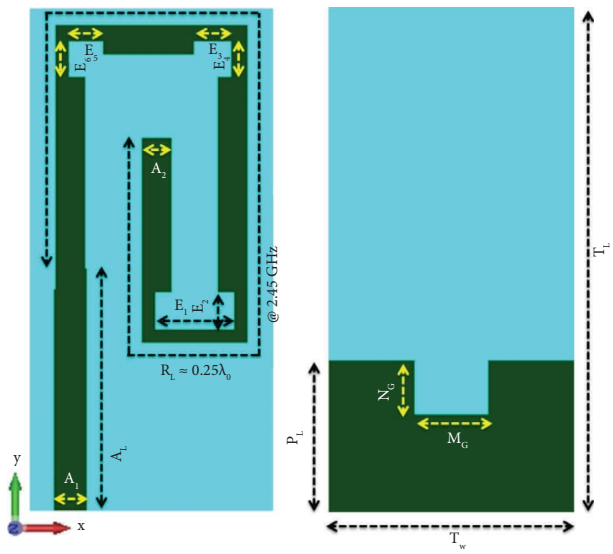

Figure 2: Design layout of the proposed antenna-sensor.

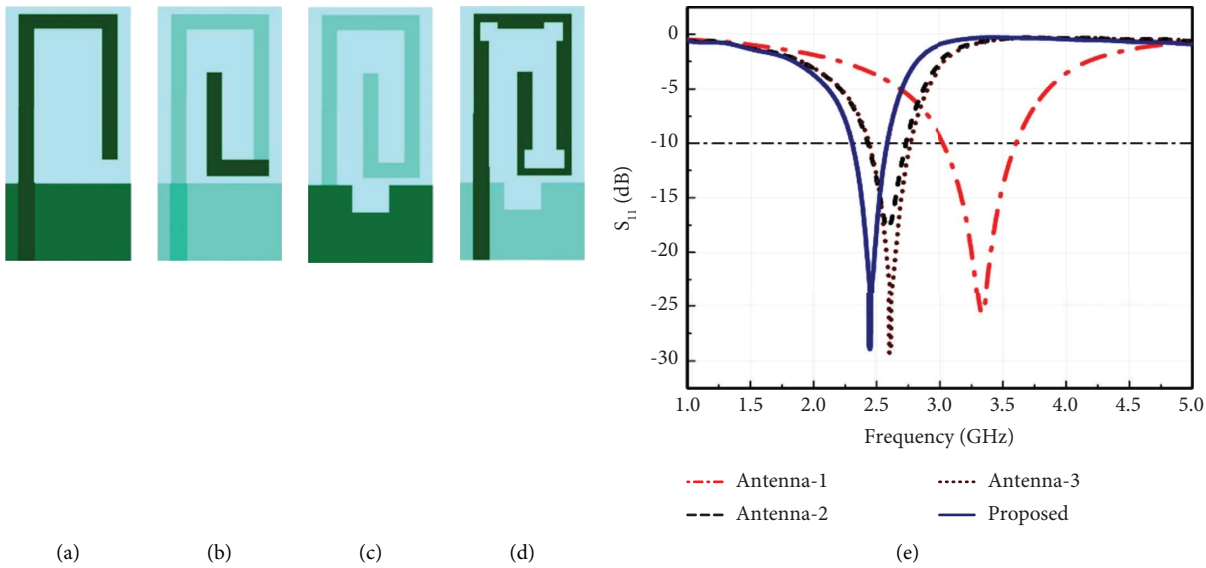

Figure 3: Design evolution of the proposed antenna-sensor: (a) antenna-1, (b) antenna-2, (c) antenna-3, (d) proposed, and (e) S_{11}-parameters for antenna-1 to proposed.

shift resonating frequency towards the desired ISM band, the electrical length of the resonator is increased using an L-shaped strip in the next stage of evolution. In the lower-end mode, the antenna structure achieves resonance at 2.58 GHz (antenna-2), as shown in Figure 3(b), and its resonating electrical length is nearly equal to the quarter wavelength [21]. By introducing a defect in the ground plane (antenna-3), as shown in Figure 3(c), good impedance matching is achieved at 2.6 GHz. Also, by adding an L-shaped strip to the resonator and a U-shaped slit in the ground plane, the resonant frequency shifts within the ISM band. The resonating behavior of antenna-3 is investigated further using surface current distribution at 2.6 GHz. Since the edges of the resonator have the highest surface current [22], rectangular slits are employed on them to achieve the desired resonance frequency of 2.45 GHz without influencing impedance matching (depicted in Figure 3(d)). A parametrical study has been carried out on each step of evolution, which is discussed in the following section. The S_{11}-parameters for the evolution of proposed antenna sensor are depicted in Figure 3(e).

2.2. Parametrical Studies. In the initial phase of evolution, antenna-1 resonates at 3.34 GHz, exhibiting a reflection coefficient of −27.2 dB. In order to enhance antenna-1's performance to align with the desired ISM band, a parametric analysis is conducted on the length of the radiating element, denoted as R_L, which plays a key role in parametric optimization. This involves adjusting the R_L value within

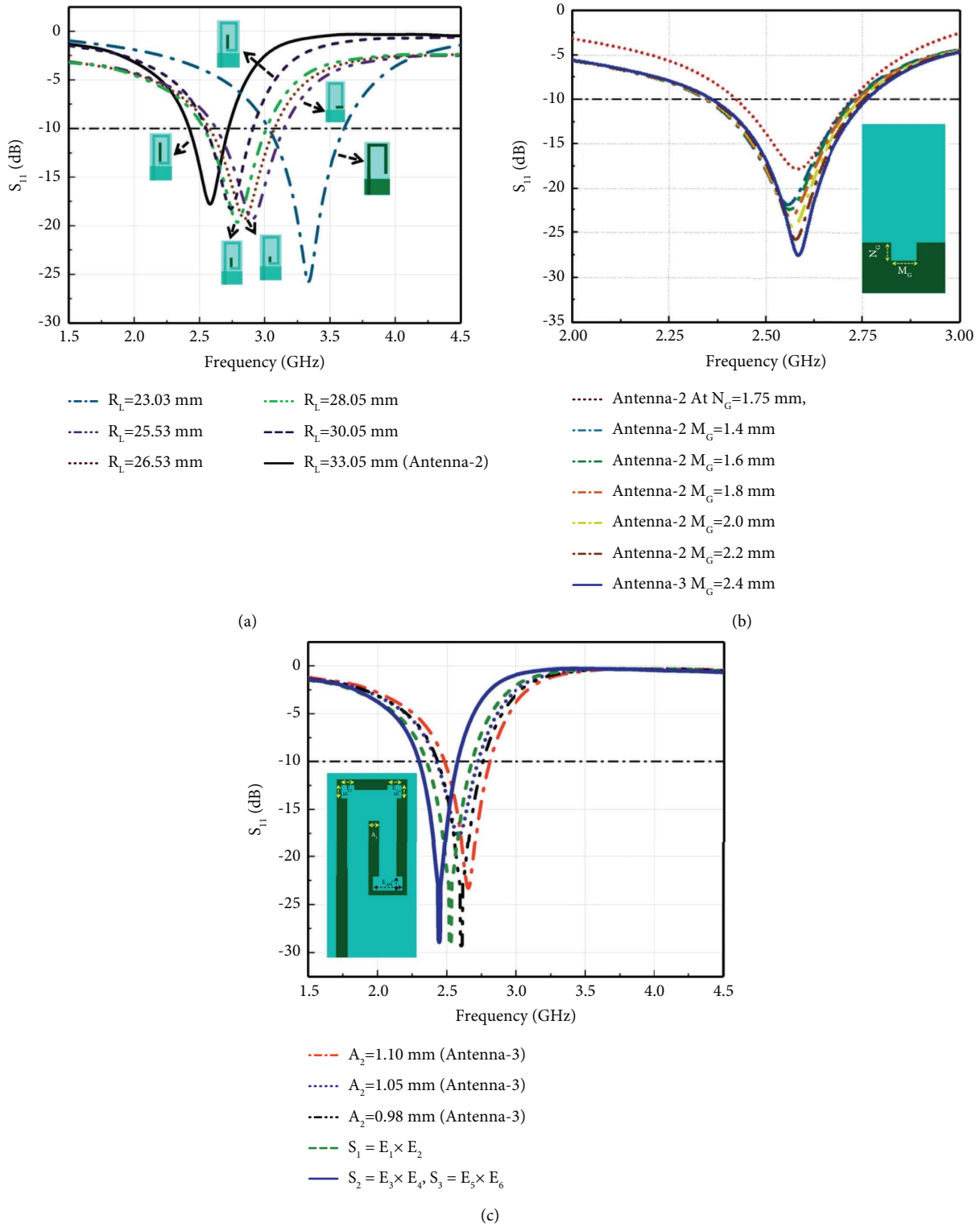

Figure 4: Parametric analysis results for critical design parameters: (a) R_L, (b) M_G, and (c) A_2.

a specified range using a full-wave simulator. Figure 4(a) illustrates the S_{11} response as a function of R_L variation, allowing us to compare it with the S_{11} response obtained in the initial evolution step. Ultimately, an R_L value of 23.03 mm is chosen, resulting in resonance at 2.58 GHz, which closely aligns with the desired ISM band.

To further improve impedance matching, a U-slot is introduced in the center of the ground plane during the second phase of evolution. This involves optimizing two parameters, namely, N_G and M_G, associated with the U-slot. By selecting $N_G = 1.75$ mm and varying the M_G value between 0 and 2.4 mm, we achieve proper impedance matching. The

modified S_{11} plot, with respect to N_G and M_G, is depicted in Figure 4(b), clearly showing the significant impact of the U-slot on S_{11} magnitude within the desired frequency band. In the next step, the width of the radiating element is adjusted by parameter A_2 (shown in Figure 4(c)). Furthermore, semi-rectangular slots are introduced in the corners of the resonator, guided by the study of surface current density. This modification results in the realization of the desired ISM band with a bandwidth of 290 MHz. The final dimensions of the proposed antenna sensor are as follows: $T_L = 16.2$ mm, $T_W = 8$ mm, $A_L = 10$ mm, $A_1 = 1.08$ mm, $R_L = 33.05$ mm, $A_2 = 0.98$ mm, $P_L = 5$ mm, $N_G = 1.75$ mm $M_G = 2.4$ mm, $E_1 = 2.6$ mm, and $E_2 = E_3 = E_4 = E_5 = E_6 = 1.2$ mm. At the operating frequency of 2.4 GHz, the antenna achieves a realized gain of 1.1 dBi and a directivity of 0.86 dBi.

2.3. Free-Space Performance. The proposed antenna sensor prototype is fabricated on the Teslin substrate of 0.35 mm thickness, as shown in Figure 5(a), and it is measured in an anechoic chamber using a vector network analyzer (Anritsu N9926A). The measured results show −10 dB impedance bandwidth of 342 MHz (2.18 GHz −2.522 GHz), with resonance at 2.413 GHz, as shown in Figure 5(b). The far-field parameters of the antenna sensor are measured inside an anechoic chamber to restrict undesired reflections. Figure 6 depicts the measured normalized radiation characteristics of the fabricated antenna prototype. The antenna sensor has a bidirectional pattern in the *yz*-plane ($\phi = 90^\circ$) and an omnidirectional pattern in the xz-plane ($\phi = 0^\circ$). The proposed antenna sensor achieved a measured gain of 0.94 dBi. The measured results slightly deviated from the simulated results. This might be due to the parasitic effect of solder, which is not properly aligned between the coaxial probe and the antenna feed position.

The electrically small antenna (ESA) characteristics of the proposed antenna sensor are further analyzed using the conditions given in [22].

$$\mathbf{ka} \leq \mathbf{0.5}, \text{ for ESA}, \tag{1}$$

where "k" is the wave number and "a" is the minimum radius of the sphere related to the distance between the antenna center and its apex. At 2.413 GHz resonating frequency, $k = 0.05$ ($k = 2\pi/\lambda_0$), where λ_0 is operating wavelength, $a = 8.97$ mm ($a = \lambda_0/13.6$), and ka = 0.44 for the proposed antenna sensor.

3. Inhomogeneous Eye Modeling and Testing

3.1. In Simulation Scenario. The SMC eye model is created with multiple biological tissues to replicate the real human eye, as shown in Figure 7. The sclera, choroid, and retina are the major outer layers of the human eye, with a sphere radius of 11-12 mm [23]. Aqueous humor covers the region between the cornea and lens, which are both inside the eyeball. The ciliary body is an outgrowth of the iris that produces aqueous humor. The brain, skull bone, muscle, fat, and skin are the other major outer tissues of the human eye. As shown in Table 2, the dielectric constant, conductivity, and density of all of these tissues are considered in the simulation to replicate the real condition at 2.45 GHz [24]. The proposed antenna sensor design takes into account the proximity of biological tissues positioned in its far field. Due to the dielectric properties of biological tissues, an antenna close to tissues will propagate differently than an antenna in free space [25].

The proposed antenna sensor's reflection parameters with the SMC eye model resonate at 2.292 GHz for a near-field distance of 3 mm and 2.38 GHz for a far-field distance of 5.35 mm. Also, the SAR is calculated to estimate the RF radiation absorbed by the SMC eye model. A system with the Intel Core i7-2600 processor and 24 GB of RAM is used for SAR calculation. In total, a single simulation run lasted approximately three hours. It is noticed during the investigation that the values of SAR do not exceed above 1.6 W/kg at far-field (5.35 mm) and near-field (3 mm) distances for 0.001 W of input power, as depicted in Figure 8. Next, a cancerous tumor with a radius of 2–3.5 mm is introduced one after the other near the choroid layer (corner of vitreous humor) of the eye to test for malignancy of the eye.

The dielectric properties of benign tumor are considered as $\epsilon_r = 61.6$ and $\sigma = 4.09$ [26]. For near-field distance (3 mm), the reflection characteristics are reviewed every 0.1 mm along the *x*- and *y*-axes (horizontal and vertical) for the single and double tumors. Then, the maximum resonant frequency shift is recorded and tabulated in Table 3.

$$\mathbf{T_s} = \mathbf{1.608} + \mathbf{0.114F_s} - \mathbf{0.0015F_s^2}. \tag{2}$$

Figure 9 depicts the polynomial curve fitting results for the single tumor-simulated S_{11}. A polynomial regression (2) with a statistical $R^2 = 0.9987$ represents the relationship between the frequency shift of the proposed antenna sensor and the size of the tumor, where Fs is the resonant frequency shift of a single tumor of the antenna sensor and Ts is the size of the tumor. It is observed that when the proposed antenna sensor is positioned at near-field distance from the SMC eye model, with single and double tumors, its resonance changes from 2.292 GHz, as shown in Figure 10.

The maximum shift of the resonance frequency for the SMC eye model with a cancerous tumor is 54 MHz. This proves that the proposed antenna sensor is sensitive to variations in the body tissues, and hence it can be used for the early detection of ocular tumors.

3.1.1. Parametric Study on Tissue Uncertainties. The proposed antenna sensor is positioned in front of an eye model. Tumors of different sizes (3 mm and 3.5 mm radius) are induced in the vitreous humor of the eye model. The key parameter being measured is the frequency shift of the proposed antenna sensor. The changes in the frequency shift are recorded. It has been observed that there is a controlled simulation setup in which the sensor is tested with tumors of known sizes and in different locations. Hence, the proposed antenna sensor for the detection of tumors within the vitreous humor of the eye model has shown promising results. The sensor effectively registered changes in the frequency shift through induced tumors of varying sizes and positions, as shown in Table 4.

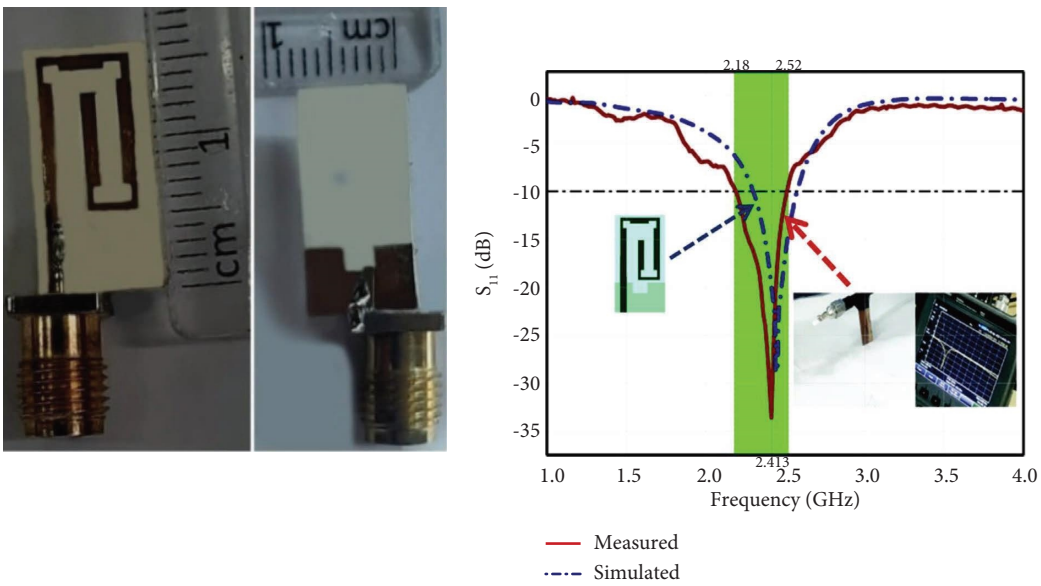

Figure 5: (a) Fabricated antenna prototype and (b) measured results of the proposed antenna-sensor.

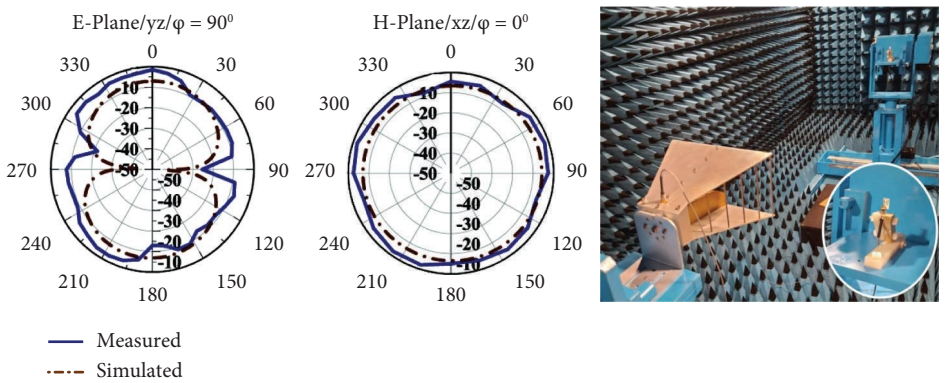

Figure 6: Far-field characteristics of the proposed antenna-sensor at 2.413 GHz.

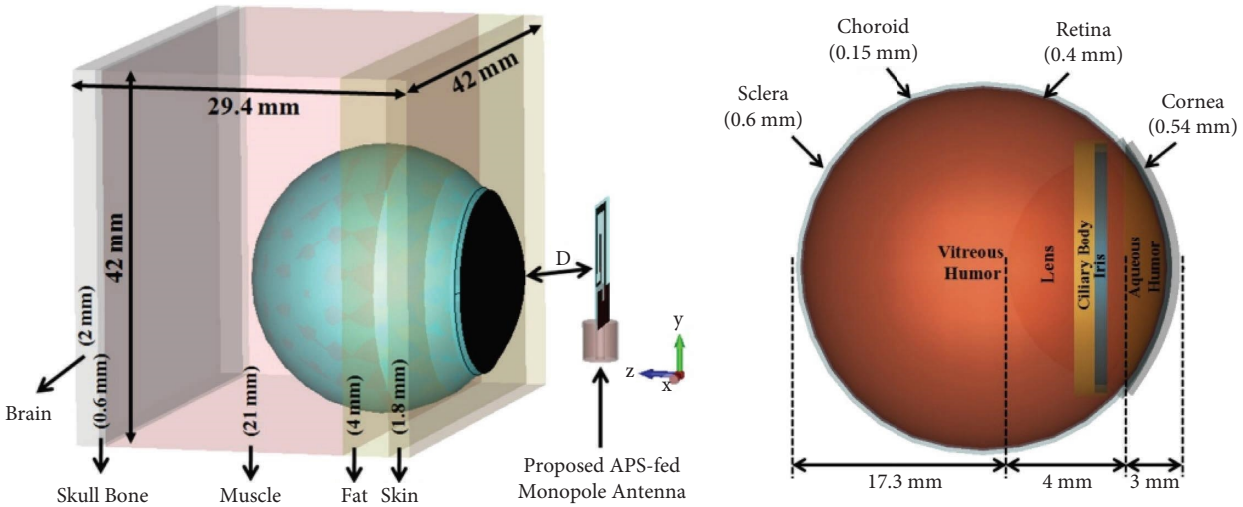

Figure 7: The simplified multilayered canonical eye model with the proposed antenna-sensor.

Table 2: Dielectric properties of biological tissues used in head and eye model at 2.4 GHz [24].

Tissue	Density (ρ) (kg/m^3)	Dielectric constant	Conductivity (σ) (S/m)
Cornea	1062	51.63	2.29
Aqueous humor	1009	66.26	3.45
Ciliary body, iris	1090	52.74	1.73
Lens	1100	33.98	1.08
Vitreous humor	1005	68.21	2.47
Retina	1039	48.95	1.8
Choroid blood	1050	58.28	2.55
Sclera	1076	52.65	2.03
Brain	1030	48.91	1.8
Skull bone	1850	11.38	0.39
Muscle	1040	52.729	1.74
Fat	920	5.28	0.11
Skin	1050	38.01	1.46

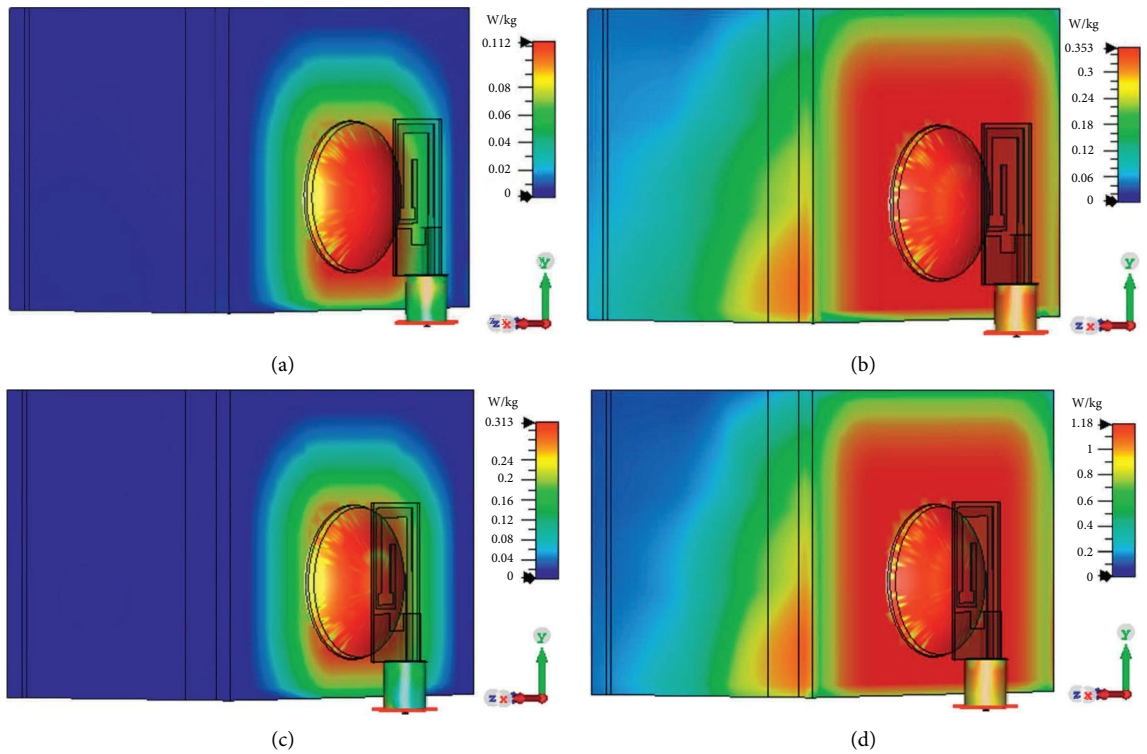

Figure 8: SAR results of the proposed antenna-sensor with the SMC eye model (a) for 1 g tissue at a far-field distance, (b) for 10 g tissue at a far-field distance, (c) for 1 g tissue at a near-field distance, and (d) for 10 g tissue at a near-field distance.

Table 3: Resonance frequency shifts for different sizes of tumors at $D = 3$ mm.

Tumor size (mm)	Single tumor		Double tumors	
	Resonating frequency (GHz)	Frequency shift (MHz)	Resonating frequency (GHz)	Frequency shift (MHz)
Absence of tumor	2.292	—	2.292	—
2	2.288	4	2.276	16
2.5	2.284	8	2.272	20
3	2.276	16	2.56	36
3.5	2.268	24	2.238	54

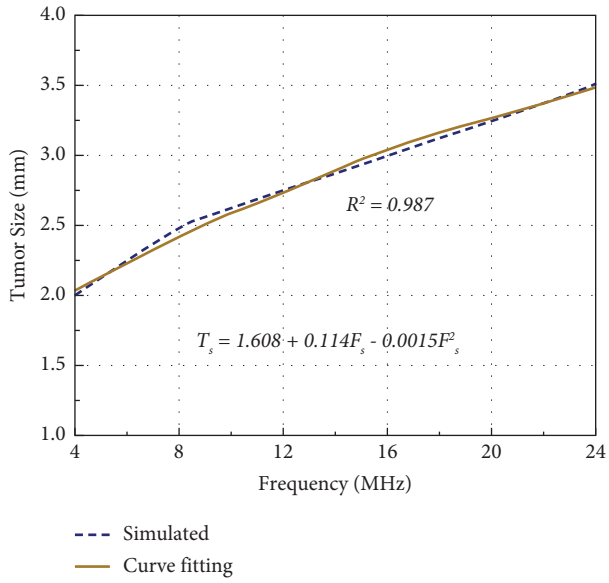

Figure 9: Curve fitting response as a function of frequency shift for a single tumor.

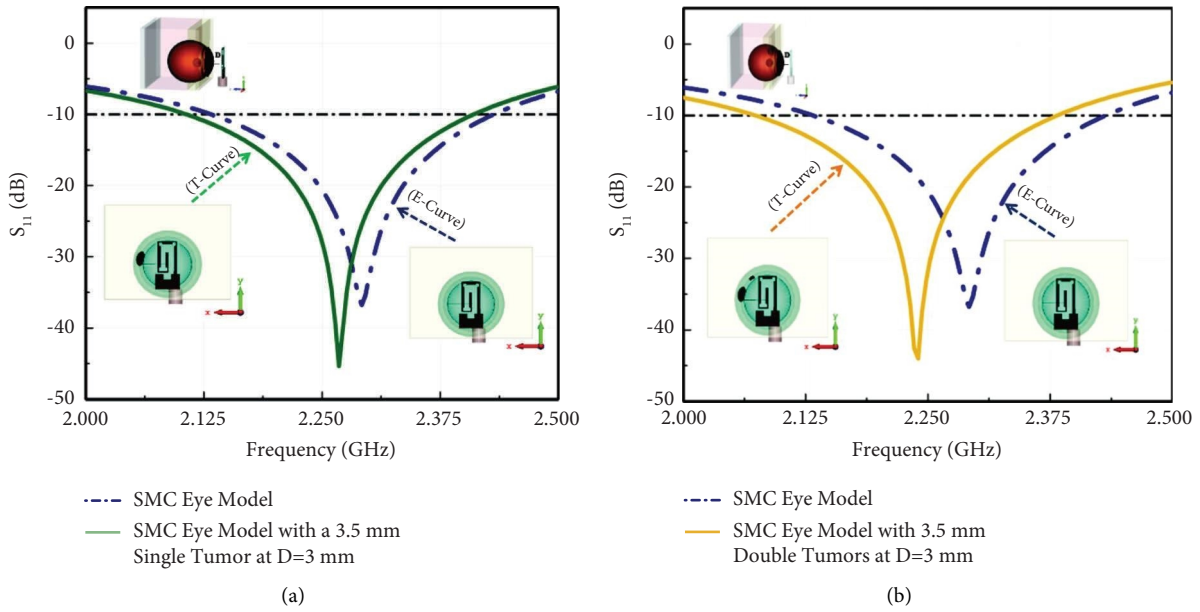

Figure 10: S_{11}-parameters of the proposed antenna-sensor with SMC eye model including cancerous (a) single tumor and (b) double tumor at $D = 3$ mm.

3.2. Eye Model Preparation and Testing. The efficacy of the proposed antenna sensor for ocular tumor detection is evaluated by validating the simulated results of the proposed antenna with measurements. To test the sensing ability of the proposed antenna, an eye phantom with a head-testing model similar to the SMC eye model is developed. The testing model depicted in Figure 11(a) is a pair of spherically shaped, semi-solid phantoms (phantom A and phantom B) with an approximate radius of 12 mm and 3.5 mm that are used to replicate eyeball vitreous humor and malignant tumor tissues, respectively. To imitate the head with eye tissues, the spherical semi-solid eyeball is submerged in a transparent plastic container ($20 \times 20 \times 8$ mm^3) containing phantom C, which is prepared using the recipe given in [24].

To replicate the approximate real-time conditions of ocular and tumor tissues, phantom A and phantom B solutions are prepared using the compositions given in [27, 28]. Triton X-100 and salt mixtures (15%, 7.4 g/L) are used for preparing vitreous humor (phantom A) due to their stable electrical properties over a long period of time and temperature, and the obtained results are $\epsilon_r = 69.2$ and $\sigma = 2.8$ S/m. A permittivity (ϵ_r) of 61.6 and conductivity (σ)

Table 4: Frequency shifts for different locations of ocular tumor with a radius of 3 and 3.5 mm

Position (x, y, z) (mm)	Tumor radius = 3 mm		Tumor radius = 3.5 mm	
	Resonating frequency (GHz)	Frequency shift (MHz)	Resonating frequency (GHz)	Frequency shift (MHz)
(0, 0, 0)	2.276	16	2.268	24
(0, 0, 2)	2.276	16	2.268	24
(0, 0, 4)	2.276	16	2.268	24
(0, 0, −2)	2.276	16	2.269	23
(0, 0, −4)	2.277	15	2.268	24
(0, 2, 0)	2.276	16	2.268	24
(0, 4, 0)	2.277	15	2.268	24
(0, −2, 0)	2.276	16	2.268	24
(0, −4, 0)	2.276	16	2.267	25
(2, 0, 0)	2.276	16	2.268	24
(4, 0, 0)	2.276	16	2.268	24
(−2, 0, 0)	2.277	15	2.268	24
(−4, 0, 0)	2.277	15	2.268	24
(0, 2, 2)	2.276	16	2.267	25
(0, 4, 4)	2.275	17	2.268	24
(0, −2, −2)	2.276	16	2.268	24
(0, −4, −4)	2.276	16	2.268	24
(2, 0, 2)	2.276	16	2.268	24
(4, 0, 4)	2.276	16	2.269	23
(−2, 0, −2)	2.276	16	2.268	24
(−4, 0, −4)	2.277	15	2.267	25
(2, 2, 0)	2.277	15	2.268	24
(4, 4, 0)	2.277	15	2.268	24
(−2, −2, 0)	2.276	16	2.269	23
−4, −4, 0)	2.276	16	2.267	25
(2, 2, 2)	2.276	16	2.268	24
(4, 4, 4)	2.276	16	2.268	24
(−2, −2, −2)	2.276	16	2.268	24
(−4, −4, −4)	2.276	16	2.269	23

of 2.2 S/m (phantom B) are obtained using mixtures of agar (1.7 g), salt (0.5844 g), deionized water (100 ml), and ethanol (60 ml). These readings resemble a cancerous tumor at 2.45 GHz.

(1) Tumor detection using frequency shift: The proposed antenna sensor is placed near the testing eye model with and without a tumor. The S_{11}-parameters are recorded using the vector network analyzer (VNA) and shown in Figures 11(b) and 11(c). It is observed that the resonance frequency of 2.36 GHz is obtained for testing the eye model without a tumor, and by including a tumor of radius of 3.5 mm, the resonance frequency shifts from 2.36 GHz to 2.29 GHz (70 MHz, for a single tumor). For double tumors, the resonance frequency shifts from 2.36 GHz to 2.24 GHz (120 MHz). It is noticed that the measured resonance frequency shift of the proposed antenna with phantoms is higher than the simulated results. These differences could be attributed to phantom mixture compositions with approximate electrical properties, slight increment of radius of the tumor, and the absence of external layers of the vitreous humor. The measured results show a significant impedance match across the proposed antenna sensor. These reflection parameters are further examined and discussed in the following using a multivariate data analysis technique, PCA.

(2) PCA on reflection parameters: The PCA is a multivariate data analysis technique, and it is used to study multiple variables in a set of data. PCA reduces a large number of variables that may be correlated into a more manageable set of principal components (PCs) using sophisticated mathematical underlying principles [29]. Therefore, by examining the reduced-dimension dataset, the user can identify trends, patterns, and outliers in the data. In this work, the dataset is considered as the reflection coefficients for 1001 frequency points of an eye phantom (E) with a tumor (T). The 1001 reflection coefficients are the variables, and E and T curves are the two observations. Hence, the tumor can be predicted by plotting the two coordinates representing the two points in 1001-dimensional space. If the observations (E and T curves) have any correlation, the correlated points are observed in the 1001-dimensional space.

In order to better understand the PCA method, it is represented in terms of its linear algebra fundamentals, and it is assumed that the dataset is represented by an $m \times n$ matrix, $\mathbf{A}$, where the m (1001) rows are the variables

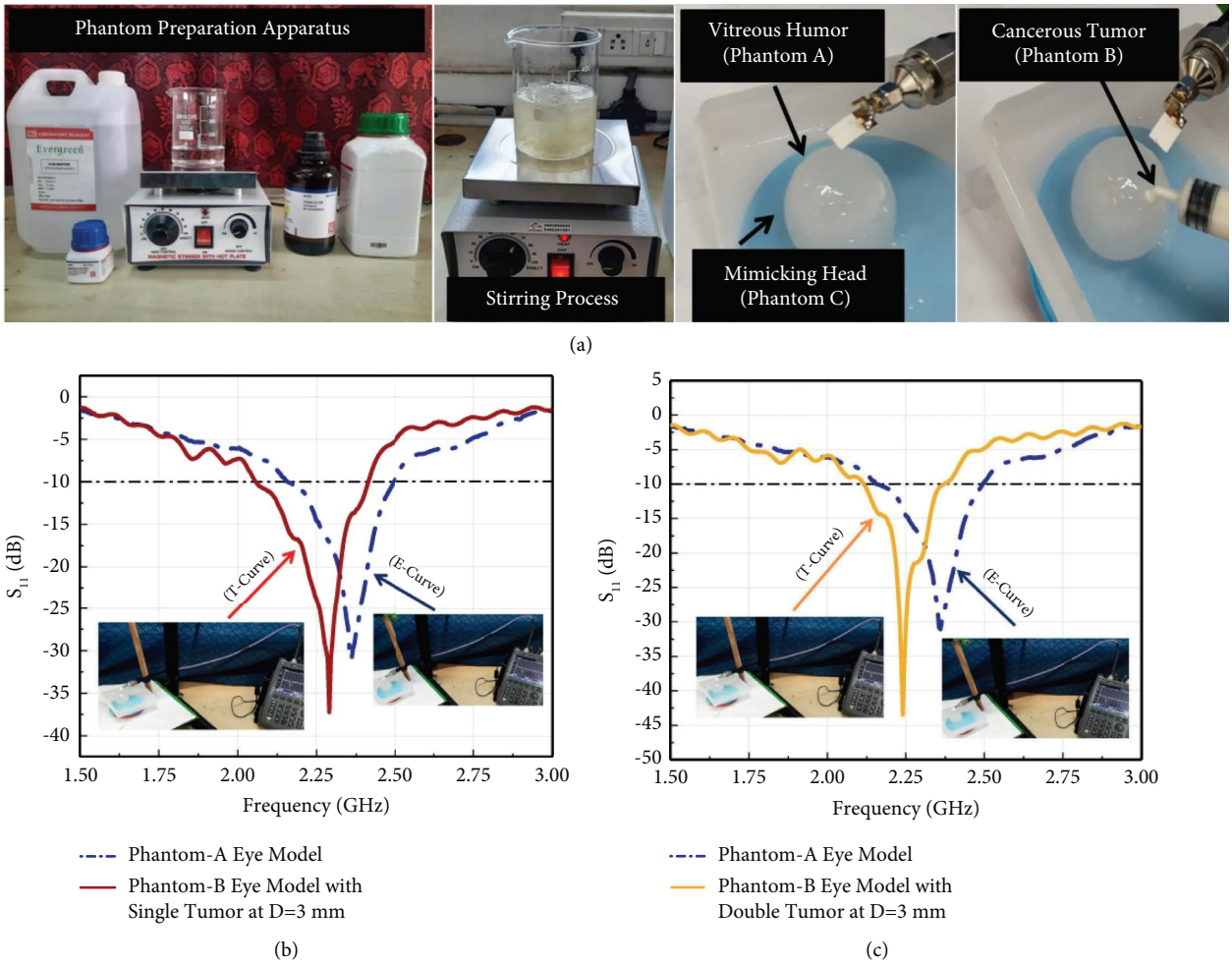

Figure 11: (a) Preparation of phantoms for experimental investigation and measured S_{11}-parameters for eye phantom with (b) single tumor and (c) double tumor.

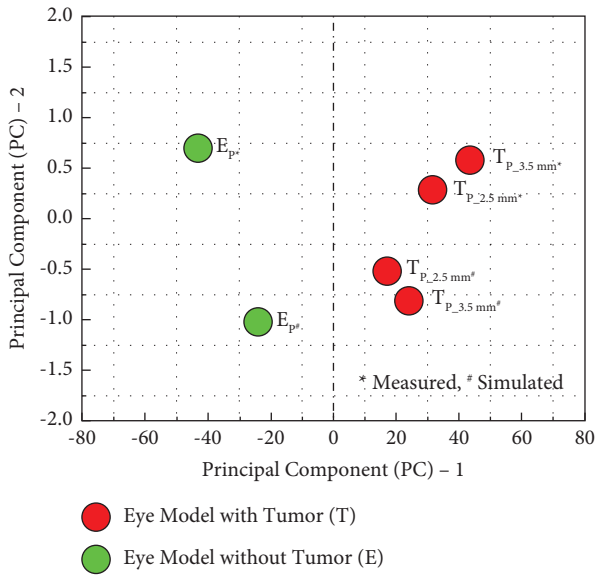

Figure 12: PCA results of eye model with and without tumor.

Table 5: Comparison of the proposed microwave antenna sensor with other diagnosis systems.

Ref. (year)	Antenna size ($W \times L \times H$) (mm^3)	Operating frequency (GHz)	Biodegradable substrate	Application	Method	Contact-less
[28] (2019)	$114 \times 80 \times 1.6$	2.4	No	Bone fracture diagnosis	Microwave imaging	No
[30] (2020)	$30 \times 40 \times 1.016$	3–7	No	Bone health evaluation	Time-domain analysis	Yes
[31] (2021)	$37 \times 37 \times 0.7$	2.4	No	Salinity and sugar concentration measurement	Frequency shifting	No
[12] (2022)	$45 \times 7.87 \times 0.46$	2.4	No	Chest wall movement detection	Frequency shifting	No
[32] (2022)	$50 \times 30 \times 0.8$	3	No	Dielectric constant measurement	Frequency shifting	No
[33] (2022)	$18.2 \times 22 \times 1.6$	5.7	No	Glucose monitoring	Time-domain analysis	Yes
This work	$8 \times 16.2 \times 0.35$	2.413	Yes	Ocular tumor detection	Frequency shifting and PCA	Yes

(reflection coefficients) and the n (2) columns are the observations.

$$\mathbf{A} = \begin{bmatrix} \mathbf{R_{E1}} & \mathbf{R_{T1}} \\ \vdots & \vdots \\ \mathbf{R_{E1001}} & \mathbf{R_{T1001}} \end{bmatrix}. \tag{3}$$

The $\mathbf{R_E}$ and $\mathbf{R_T}$ are reflection coefficients belongs to **E and T curves**. The linear transformation of matrix **A** into matrix **B** with matrix **P** of dimensions $\mathbf{m \times m}$ is

$$\begin{aligned} \mathbf{B} &= \mathbf{PA} \\ &= \begin{bmatrix} \mathbf{P_1}.\mathbf{R_{E1}} & \mathbf{P_1}.\mathbf{R_{T1}} \\ \vdots & \vdots \\ \mathbf{P_{1001}}.\mathbf{R_{E1001}} & \mathbf{P_{1001}}.\mathbf{R_{T1001}} \end{bmatrix}. \end{aligned} \tag{4}$$

In (4), matrix **A** is projected onto **P** columns to determine the principal component directions. The following step uses the variance property $\boldsymbol{\sigma_X^2} = (\mathbf{1/n-1})\mathbf{XX^T}$ to determine how much two variables change together. Also, some features must be chosen for the transform matrix, **B**, and must relate them to the features of the corresponding covariance matrix, $\mathbf{C_B}$.

$$\begin{aligned} \mathbf{C_B} &= \frac{\mathbf{1}}{\mathbf{n-1}}\mathbf{BB^T} \\ &= \frac{\mathbf{1}}{\mathbf{n-1}} \begin{bmatrix} \mathbf{B_1}\mathbf{B_1^T} & \cdots & \mathbf{B_1}\mathbf{B_{1001}^T} \\ \vdots & \ddots & \vdots \\ \mathbf{B_{1001}}\mathbf{B_1^T} & \cdots & \mathbf{B_{1001}}\mathbf{B_{1001}^T} \end{bmatrix}. \end{aligned} \tag{5}$$

The variances are observed on both the diagonal and off-diagonal entries of the above matrix when its entries are closely examined. Therefore, the transformation matrix **P** can be chosen so that $\mathbf{C_B}$ is diagonal in order to estimate the potential covariance between the two observations.

$$\begin{aligned} \mathbf{C_B} &= \frac{\mathbf{1}}{\mathbf{n-1}}\mathbf{BB^T} \\ &= \frac{\mathbf{1}}{\mathbf{n-1}}\mathbf{PA}(\mathbf{PA})^{\mathbf{T}} \\ &= \frac{\mathbf{1}}{\mathbf{n-1}}\mathbf{P}\left(\mathbf{AA^T}\right)\mathbf{P^T}, \\ \mathbf{C_B} &= \frac{\mathbf{1}}{\mathbf{n-1}}\mathbf{PXP^T}, \end{aligned} \tag{6}$$

where $\mathbf{X} = \mathbf{AA^T}$. It should be noted that **X** is a symmetric matrix, $m \times m$, and that every square symmetric matrix is orthogonally diagonalisable according to linear algebra, i.e.,

$$\mathbf{X} = \mathbf{EFE^T}, \tag{7}$$

where **F** is a diagonal matrix whose (diagonal) entries are the eigenvalues of **X** and **E** is an orthonormal matrix, $\mathbf{m \times m}$, whose columns are the orthonormal eigenvectors of **X**. Finally, by selecting the rows of **P** to be the eigenvectors of **X**, it is ensured that $\mathbf{P} = \mathbf{E^T}$ and vice versa. Thus, the expression for the covariance matrix, $\mathbf{C_B}$, becomes

$$\begin{aligned} \mathbf{C_B} &= \frac{\mathbf{1}}{\mathbf{n-1}}\mathbf{PXP^T} \\ &= \frac{\mathbf{1}}{\mathbf{n-1}}\mathbf{E^T}\left(\mathbf{EFE^T}\right)\mathbf{E}. \end{aligned} \tag{8}$$

Since $\mathbf{EE^T} = \mathbf{I}$ (identity matrix),

$$\begin{aligned} \mathbf{C_B} &= \frac{\mathbf{1}}{\mathbf{n-1}}\mathbf{F} \\ &= \begin{bmatrix} \mathbf{PC_{1E}} & \mathbf{PC_{1T}} \\ \vdots & \vdots \\ \mathbf{PC_{1001E}} & \mathbf{PC_{1001T}} \end{bmatrix}, \end{aligned} \tag{9}$$

where $\mathrm{PC_{1E}}$ and $\mathrm{PC_{1T}}$ are the first PCs (highest feature) of the E- and T-curves. Using (9), the variances can be automatically extracted from the data regarding the relative significance of each principal component. The highest variance is the first principal component, followed by the second principal component, and so on. Therefore, the above-described PCA approach is coded in MATLAB with simulated and measured results, and the resulting plots are shown in Figure 12. Observe that a variable $\mathbf{E_p}$ is located on the negative side of the PC-1 axis and $\mathbf{T_p}$ is located on the positive side of the PC-1 axis, and they are clustered together, whereas $\mathbf{T_p}$ cluster is the PC belonging to an eye phantom with a single tumor (2.5 mm and 3.5 mm) and is located away from the $\mathbf{E_p}$ cluster (PCs belonging to eye phantom without tumor).

As a result, the PCA can generate these correlations. It has significantly lowered the size of the dataset from 1001 to 2, allowing one to assert (as shown in Figure 12) that healthy phantoms and tumors are different PCs. The frequency shift analysis and PCA technique employ simulated and measured reflection coefficients and are more impactful in distinguishing between healthy and malignant tissues. Both frequency shift analysis and PCA are effective at detecting tumors inside the eyes. Table 5 shows the performance comparison of the proposed microwave antenna sensor with other recent antenna systems. In comparison to previously reported antennas, the proposed antenna sensor has a meandered monopole design that results in a small geometry, is designed on a biodegradable substrate, is contactless, and uses machine learning for the accurate detection of ocular tumors.

4. Conclusion

An asymmetric planar strip-fed monopole antenna sensor is designed and developed to detect ocular tumors. Its implementation is close to the fundamental physical limits of ESAs found in the literature due to its smaller size ($\lambda_0/15.3 \times \lambda_0/7.5 \times \lambda_0/350$). Near-field and far-field results are discussed along with the SAR computations for the input

power of 10 dBm. The proposed antenna sensor is fabricated on a Teslin paper substrate and tested with an eye-mimicking phantom to compare numerical computations with measurements. In addition, the reflection parameters are analyzed using PCA for the accuracy of tumor detection. Compared to the previously reported works, the proposed diagnostic system has several advantages, such as a non-invasive mechanism, portability, and wearable biodegradable substrate, and a planar antenna for ocular tumor detection is hardly reported. Therefore, the proposed small-size antenna sensor could be a viable solution in the portable diagnosis system for the early detection of cancerous tumors in the eye. Although the results of the proposed antenna sensor are the first of their kind, further advancements in the detection algorithms are still required [34].

Data Availability

The data used to support the findings of this study are available from the corresponding authors upon request.

Conflicts of Interest

The authors declare that they have no conflicts of interest.

References

[1] R. Leclerc and J. Olin, "An overview of retinoblastoma and enucleation in pediatric patients," *AORN Journal*, vol. 111, no. 1, pp. 69–79, 2020.

[2] cancer, "American cancer society's estimates for eye cancer in the united states for 2022," 2022, https://www.cancer.org/cancer/eyecancer/about/key-statistics.html.

[3] J. Wang, H. Chen, X. Wu, and L. Tang, "Comparison of diagnostic efficiency of breast cancer imaging in Chinese women: digital mammography, ultrasound, MRI, and combinations of these modalities," *Journal of Medical Imaging and Health Informatics*, vol. 5, no. 7, pp. 1488–1493, 2015.

[4] M. Kriege, C. T. Brekelmans, C. Boetes et al., "Efficacy of MRI and mammography for breast-cancer screening in women with a familial or genetic predisposition," *New England Journal of Medicine*, vol. 351, no. 5, pp. 427–437, 2004.

[5] E. Dougeni, K. Faulkner, and G. Panayiotakis, "A review of patient dose and optimisation methods in adult and paediatric CT scanning," *European Journal of Radiology*, vol. 81, no. 4, pp. 665–683, 2012.

[6] G. Tsokolas, K. T. Tsaousis, V. F. Diakonis, A. Matsou, and S. Tyradellis, "Optical coherence tomography angiography in neurodegenerative diseases: a review," *Eye and Brain*, vol. 12, pp. 73–87, 2020.

[7] M. E. Brezinski, "Capabilities, limitations, and misconceptions of using OCT to assess vulnerable plaques," *Nature Reviews Cardiology*, vol. 11, p. 638, 2014.

[8] D. P. Popescu, L. Choo-Smith, C. Flueraru et al., "Optical coherence tomography: fundamental principles, instrumental designs and biomedical applications," *Biophysical reviews*, vol. 3, no. 3, pp. 155–169, 2011.

[9] F. R. Kareem, A. A. Ibrahim, and M. A. Abdalla, "Triple band monopole textile wearable antenna for IoMT application," *IEEE Sensors Journal*, vol. 23, no. 19, pp. 23377–23387, 2023.

[10] Y. Mahnashi, K. K. Qureshi, A. A. Al-Shehri, and H. Attia, "Design and experimental validation of a noninvasive glucose monitoring system using RF antenna-based biosensor," *IEEE Sensors Journal*, vol. 23, no. 3, pp. 2856–2864, 2023.

[11] S. Gundapaneni, G. S. N. Raju, and A. S. D. Pendurthi, "Inverted Ω-shaped antenna for 2.45 GHz ISM band wearable applications," *Iranian Journal of Science and Technology, Transactions of Electrical Engineering*, vol. 47, no. 3, pp. 1177–1186, 2023.

[12] A. B. Dey, N. Semwal, and W. Arif, "Design of a compact and efficient 2.4 GHz rectenna system for energy harvesting," *Journal of Electromagnetic Waves and Applications*, vol. 36, no. 13, pp. 1850–1868, 2022.

[13] A. V. Boologam, K. Krishnan, S. K. Palaniswamy et al., "On the design and development of planar monopole antenna for bone crack/void detection," *International Journal of Antennas and Propagation*, vol. 2022, pp. 1–12, 2022.

[14] M. El Gharbi, R. Fernández-García, I. Gil, and I. Gil, "Embroidered wearable antenna based sensor for real-time breath monitoring," *Measurement*, vol. 195, Article ID 111080, 2022.

[15] J. Padhi, A. Kumar, and G. S. Reddy, "Parasitic element loaded efficient electrically small antenna for indoor wireless applications," *Microwave and Optical Technology Letters*, vol. 64, no. 10, pp. 1793–1799, 2022.

[16] P. N. Pillai and R. Pandeeswari, "Electrically small asymmetric coplanar strip-fed metamaterial-inspired antenna for wlan and satellite-based applications," *Microwave and Optical Technology Letters*, vol. 65, 2022.

[17] E. M. Ali, W. A. Awan, S. I. Naqvi et al., "A low-profile antenna for on-body and off-body applications in the lower and upper ISM and WLAN bands," *Sensors*, vol. 23, no. 2, p. 709, 2023.

[18] M. C. YunusEmre and S. CumhurBasaran, "Miniaturized multiband implantable antenna designs for in-body compact medical devices," *International Journal of RF and Microwave Computer-Aided Engineering*, vol. 32, no. 11, 2022.

[19] M. H. B. Ucar and E. Uras, "A compact modified two-arm rectangular spiral implantable antenna design for ISM band biosensing applications," *Sensors*, vol. 23, no. 10, p. 4883, 2023.

[20] M. H. B. Ucar and E. Uras, "Multilayer Archimedean spiral antenna design for dual-band intra-arm implantable biotelemetric smart health care monitoring system covering MICS and ISM bands," *Frequenz*, vol. 76, no. 7-8, pp. 441–452, 2022.

[21] J. S. G. Hong and M. J. Lancaster, *Microstrip Filters for RF/microwave Applications*, John Wiley Sons, Hoboken, NY, USA, 2004.

[22] D. M. Pozar, *Microwave Engineering*, John Wiley & Sons, Hoboken, NY, USA, 2011.

[23] M. Yuan, R. Das, R. Ghannam et al., "Electronic contact lens: a platform for wireless health monitoring applications," *Advanced Intelligent Systems*, vol. 2, no. 4, Article ID 1900190, 2020.

[24] V. Kaim, B. K. Kanaujia, S. Kumar, H. C. Choi, K. W. Kim, and K. Rambabu, "Electrically small circularly polarized UWB intraocular antenna system for retinal prosthesis," *IEEE Transactions on Biomedical Engineering*, vol. 69, no. 11, pp. 3504–3515, 2022.

[25] H. Bahramiabarghouei, E. Porter, A. Santorelli, B. Gosselin, M. Popovic, and L. A. Rusch, "Flexible 16 antenna array for microwave breast cancer detection," *IEEE Transactions on Biomedical Engineering*, vol. 62, no. 10, pp. 2516–2525, 2015.

[26] Y. Cheng and M. Fu, "Dielectric properties for non-invasive detection of normal, benign, and malignant breast tissues

using microwave theories," *Thoracic cancer*, vol. 9, no. 4, pp. 459–465, 2018.

[27] N. Joachimowicz, C. Conessa, T. Henriksson, and B. Duchene, "Breast phantoms for microwave imaging," *IEEE Antennas and Wireless Propagation Letters*, vol. 13, pp. 1333–1336, 2014.

[28] S. Garcıa-Jimeno, R. Ortega Palacios, M. F. Cepeda Rubio, A. Vera, L. Leija, and J. Estelrich, "Improved thermal ablation efficacy using magnetic nano particles: a study in tumor phantoms," *Progress in Electromagnetics Research*, vol. 128, pp. 229–248, 2012.

[29] J. Lever, M. Krzywinski, and N. Altman, "Principal component analysis," *Nature Methods*, vol. 14, no. 7, pp. 641-642, 2017.

[30] S. Ruchi Kerketta and D. Ghosh, "Microwave sensing for human bone health evaluation," *AEU-International Journal of Electronics and Communications*, vol. 127, Article ID 153469, 2020.

[31] M. E. Gharbi, M. Martinez-Estrada, R. Fern andez-Garcıa, and I. Gil, "Determination of salinity and sugar concentration by means of a circular-ring monopole textile antenna-based sensor," *IEEE Sensors Journal*, vol. 21, no. 21, pp. 23 751–823 760, 2021.

[32] P. V elez, F. Mart ın, R. Fern andez-Garcıa, and I. Gil, "Embroidered textile frequency-splitting sensor based on stepped-impedance resonators," *IEEE Sensors Journal*, vol. 22, no. 9, pp. 8596–8603, 2022.

[33] Y. Mahnashi, K. K. Qureshi, A. Al-Shehri, and H. Attia, "Design and experimental validation of a non-invasive glucose monitoring system using RF antenna-based biosensor," *IEEE Sensors Journal*, vol. 23, no. 3, pp. 2856–2864, 2023.

[34] V. S. Ramalingam, M. Kanagasabai, and E. F. Sundarsingh, "A compact microwave device for fracture diagnosis of the human tibia," *IEEE Transactions on Components, Packaging, and Manufacturing Technology*, vol. 9, no. 4, pp. 661–668, 2019.